




OPEN

High-frequency spin torque oscillation in orthogonal magnetization disks with strong biquadratic magnetic coupling

C. Liu , Y. Kurokawa, N. Hashimoto, T. Tanaka & H. Yuasa

In this study, we numerically investigate the spin transfer torque oscillation (STO) in a magnetic orthogonal configuration by introducing a strong biquadratic magnetic coupling. The orthogonal configuration consists of top and bottom layers with in-plane and perpendicular magnetic anisotropy sandwiching a nonmagnetic spacer. The advantage of an orthogonal configuration is the high efficiency of spin transfer torque leading a high STO frequency; however, maintaining the STO in a wide range of electric current is challenging. By introducing biquadratic magnetic coupling into the orthogonal structure of FePt/spacer/Co₉₀Fe₁₀, Ni₈₀Fe₂₀ or Ni, we were able to expand the electric current region in which the stable STO is realized, resulting in a relatively high STO frequency. For example, approximately 50 GHz can be achieved in an Ni layer at a current density of 5.5×10^7 A/cm². In addition, we investigated two types of initial magnetic state: out-of-plane and in-plane magnetic saturation; this leads to a vortex and an in-plane magnetic domain structure after relaxation, respectively. The transient time before the stable STO was reduced to between 0.5 and 1.8 ns by changing the initial state from out-of-plane to in-plane.

Ever since it was discovered that magnetization dynamics can be controlled by spin transfer torque (STT)^{1,2}, the approach has been widely studied and applied in data storage and memory applications, such as microwave-assisted magnetic recording (MAMR) in hard disk drives (HDDs) and magnetoresistive random access memory (MRAM)^{3–8}. Recently, STO is also gathering expectations for neural networks applications^{9–11}. While typical ferromagnetic transition metals show spin torque oscillation (STO) frequencies of several GHz^{12–15}, antiferromagnets are presumed to have STO frequencies in the THz region; this assumption is in light of various theoretical studies, including those on magnetic resonance frequency^{16–29}. However, usable STOs have never been achieved experimentally in antiferromagnets because of the strong exchange coupling between neighboring ions. Therefore, artificial magnetic structures such as synthetic antiferromagnetic coupling layers^{30–32} and quasi-antiferromagnets comprising biquadratic magnetic coupling^{33,34} have been proposed as an alternative to increase the STO frequency. On the other hand, an orthogonal magnetization multilayer comprising in-plane and perpendicular anisotropic magnetic layers was reported to have a high spin transfer efficiency that allows an STO to be excited easily, suggesting a spin transfer torque oscillator with high frequency and low power consumption^{35–42}. The high efficiency of the STT originates from the small angle between the magnetizations of the two magnetic layers, which unfortunately reduces the current density range that shows a stable STO, considering magnetization switching occurs frequently. Therefore, a biquadratic magnetic coupling^{33,34,43–55} was introduced between the two magnetic layers in the orthogonal configuration to suppress complete magnetization switching, thereby improving the stability of the STO. Biquadratic magnetic coupling is an interlayer exchange interaction between two ferromagnetic (FM) layers separated by a thin spacer. In general, the magnetic coupling energy E is expanded to a higher-order equation by considering the quadratic term as $E = -A_{12}\mathbf{M}_1 \cdot \mathbf{M}_2 - B_{12}(\mathbf{M}_1 \cdot \mathbf{M}_2)^2$, where \mathbf{M}_1 and \mathbf{M}_2 are the unit magnetizations in the first and second FM layers, respectively, and A_{12} and B_{12} are the bilinear and biquadratic coupling coefficients, respectively. A_{12} contributes to 0° or 180° magnetic coupling, whereas B_{12} contributes to +/−90° magnetic coupling. Typically, +/−90° coupling is realized under the conditions of $|A_{12}| < 2|B_{12}|$ and $B_{12} < 0$, using a suitable layer as a spacer. The values of A_{12} and B_{12} depend on the spacer layer material and the magnetic material, respectively, and values of 0 erg/cm² to −0.24 erg/cm² for A_{12} and −0.005 erg/cm² to −2.0 erg/cm² for B_{12} have been reported^{33,34,43–55}. Previously, we reported that biquadratic coupling

Graduate School and Faculty of Information Science and Electrical Engineering, Kyushu University, Fukuoka 819-0395, Japan. ✉email: liu.chuhan.354@s.kyushu-u.ac.jp

simply works as an effective field and increases the STO frequency in the quasi-antiferromagnet $\text{Co}_{90}\text{Fe}_{10}$ ^{33,34}. However, the frequency was limited to 15 GHz under a realistic current density, using a multilayer with two in-plane magnetization layers. After that, we reported that a high frequency was obtained by applying biquadratic coupling to an orthogonal configuration, but there were still remained issues of frequency stability and long transient time⁴². In this study, we report a numerical experiment of STO behavior in an orthogonal magnetization configuration with biquadratic coupling. Additionally, we investigate the initial state to obtain a fast response with a short transient time before the stable STO occurs.

Methods

Calculation model. The magnetization dynamics were investigated by solving the Landau–Lifshitz–Gilbert (LLG) equation with an STT term, given by

$$\frac{d\mathbf{m}}{dt} = -\gamma(\mathbf{m} \times \mathbf{H}_{\text{eff}}) + \alpha\left(\mathbf{m} \times \frac{d\mathbf{m}}{dt}\right) - \frac{g\mu_B J p}{M_s d_i e}(\mathbf{m} \times (\mathbf{m}_p \times \mathbf{m})) \tag{1}$$

where \mathbf{m} and \mathbf{m}_p are the normalized magnetization of the top free layer and bottom pinned layer, respectively, γ is the gyromagnetic ratio, α is the damping constant, g is the gyromagnetic splitting factor, μ_B is the Bohr magneton, J is the current density, p is the polarity of current, M_s is the saturation magnetization of the top layer, d_i is the thickness of the top layer, and \mathbf{H}_{eff} is the effective field, which consists of the following fields: $\mathbf{H}_{\text{eff}} = \mathbf{H}_K + \mathbf{H}_{\text{exf}} + \mathbf{H}_{\text{ex}} + \mathbf{H}_{\text{ST}} + \mathbf{H}_{\text{bq}} + \mathbf{H}_{\text{bl}}$, where \mathbf{H}_K is the magnetic anisotropy field, \mathbf{H}_{exf} is the external magnetic field, \mathbf{H}_{ex} is the exchange coupling field determined by the exchange stiffness constant A , \mathbf{H}_{ST} is the stray field that depends on the saturation magnetization of the magnetic material, \mathbf{H}_{bq} is the biquadratic exchange field determined by the biquadratic coefficient B_{12} , and \mathbf{H}_{bl} is the bilinear exchange field determined by the bilinear coefficient A_{12} . When the two ferromagnetic (FM) layers, i and j , have normalized magnetizations m_i and m_j , respectively, the bilinear and biquadratic exchange fields \mathbf{H}_{bl} and \mathbf{H}_{bq} are given by⁵⁶

$$\mathbf{H}_{\text{bl},i} = \frac{A_{12}}{\mu_0 M_{s,i} d_i} \mathbf{m}_j$$

and

$$\mathbf{H}_{\text{bq},i} = \frac{2B_{12}}{M_{s,i} d_i} \begin{bmatrix} m_{i,x} m_{j,x}^2 + m_{j,x} (m_{i,y} m_{j,y} + m_{i,z} m_{j,z}) \\ m_{i,y} m_{j,y}^2 + m_{j,y} (m_{i,x} m_{j,x} + m_{i,z} m_{j,z}) \\ m_{i,z} m_{j,z}^2 + m_{j,z} (m_{i,x} m_{j,x} + m_{i,y} m_{j,y}) \end{bmatrix} \text{ with } i \neq j \tag{2}$$

where $M_{s,i}$ is the saturation magnetization of the magnetic material of the top layer. The xy plane and z -axis are the in-plane and perpendicular directions, respectively, as shown in Fig. 1.

In the orthogonal configuration, the top and bottom FM layers are assumed to be i and j with in-plane and perpendicular magnetic anisotropy, respectively. The bilinear exchange field $\mathbf{H}_{\text{bl},i}$ is parallel to the magnetization \mathbf{m}_j , and the biquadratic exchange field $\mathbf{H}_{\text{bq},i}$ becomes

$$\mathbf{H}_{\text{bq},i} = \frac{2B_{12}}{M_{s,i} d_i} \begin{bmatrix} 0 \\ 0 \\ m_{i,z} \end{bmatrix} \tag{3}$$

This indicates that \mathbf{H}_{bq} is parallel to \mathbf{m}_j for $B_{12} > 0$ and antiparallel to \mathbf{m}_j for $B_{12} < 0$. Because the biquadratic magnetic coupling becomes apparent under the condition $B_{12} < 0$, the direction of \mathbf{H}_{bq} is parallel or opposite to \mathbf{m}_j when the biquadratic exchange magnetic coupling is realized. Here, the STT term is parallel to \mathbf{m}_j in the LLG equation, so that the biquadratic exchange coupling \mathbf{H}_{bq} is in the opposite direction to the STT. Considering that \mathbf{H}_{bq} is dominant in the effective field \mathbf{H}_{eff} as well as \mathbf{H}_{ST} , the biquadratic exchange coupling \mathbf{H}_{bq} is important for suppressing the complete magnetization reversal from the in-plane to the perpendicular direction, resulting in a stable STO. The magnetic moment of the top layer is expected to exhibit a gyro motion around the z -axis.

In the proposed model, the orthogonal configuration consisted of FePt 2 nm/spacer 2 nm/ $\text{Co}_{90}\text{Fe}_{10}$, $\text{Ni}_{80}\text{Fe}_{20}$ or Ni 2 nm. The device was disk-shaped with a diameter of 320 nm. The bottom layer of FePt had a perpendicular anisotropy, with $H_K = 15,000$ Oe and saturation magnetization $M_s = 800$ emu/cc^{57,58}. The bottom FM layer

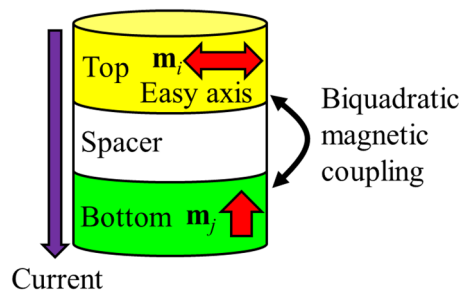


Figure 1. Calculation model with an orthogonal structure.

(j) has the fixed magnetization by setting $m_{j,x} = m_{j,y} = 0$, and $m_{j,z} = 1$ and as the current flows through its huge \mathbf{H}_k to maintain perpendicular magnetization. The top layer had an in-plane magnetic anisotropy: $\text{Co}_{90}\text{Fe}_{10}$ had $\mathbf{H}_k = 35$ Oe, $M_s = 1450$ emu/cc³³ and a damping constant α of 0.035; $\text{Ni}_{80}\text{Fe}_{20}$ had $\mathbf{H}_k = 2$ Oe, $M_s = 825$ emu/cc and a damping constant α of 0.008⁵⁹; and Ni had $\mathbf{H}_k = 2$ Oe, $M_s = 510$ emu/cc and a damping constant α of 0.0088⁶⁰. The bilinear coefficient A_{12} was set as 0 for simplicity and the biquadratic coefficient B_{12} was set to -0.6 , where B_{12} was reported in the experimental value of the spacer Fe-O³³. Both A_{12} and B_{12} are realistic values from reports so far^{33,34,43–55}. The magnetic unit cell size was $5\text{ nm} \times 5\text{ nm} \times 2\text{ nm}$, and $64 \times 64 \times 3$ cells were calculated. The exchange stiffness constant A was 1×10^{-6} erg/cm and the gyromagnetic ratio γ was 1.76×10^7 Oe⁻¹ s⁻¹. The calculation step dt was 10 fs.

In the first step, we calculated the magnetization relaxation after saturating the magnetization along the z - and y -axes. Then, the current was made to flow through the layers, from the top to the bottom layer. Because the required current density for the STO generally depends on the saturation magnetization M_s , we varied the current density from 8.0×10^7 A/cm² to 20.0×10^7 A/cm² for the $\text{Co}_{90}\text{Fe}_{10}$ top layer, and from 0.5×10^7 A/cm² to 6.0×10^7 A/cm² for the $\text{Ni}_{80}\text{Fe}_{20}$ and Ni top layers.

Results and discussion

Static and dynamic properties with z -axis magnetization saturation in initial state. First, we calculated the magnetization relaxation subject to the initial condition that the magnetization of the top layer was out-of-plane, *i. e.*, in the z -axis, as shown in Fig. 2a. Figure 2b–d show the calculated magnetization maps after relaxation in the top layers of $\text{Co}_{90}\text{Fe}_{10}$, $\text{Ni}_{80}\text{Fe}_{20}$, and Ni, respectively. Figure 2e–g show the side views of the magnetization configuration of the top and bottom layers, which correspond to the areas surrounded by black lines in Fig. 2b–d, where all magnetizations in the y -direction were superimposed on each x position. Neither external fields nor electrical currents were applied here. In this case, the exchange stiffness energy acted equally on the magnetizations of adjacent cells, causing the relaxed state of the top layer to become a vortex state, as shown in Fig. 2b–d. The bottom layer of FePt exhibited perpendicular magnetization owing to the sufficiently high perpendicular anisotropy energy.

In the next step, the current flowed through the device from the top to the bottom layers. Figure 3a–c show the [(i)–(iii)] time-domain magnetization precession, [(iv)–(vi)] Fast Fourier transform (FFT) spectra, and [(vii)–(ix)] side views of the magnetization configuration of the top and bottom layers at 20 ns after the current flow, when B_{12} is 0.0 or -0.6 for (a) $\text{Co}_{90}\text{Fe}_{10}$, (b) $\text{Ni}_{80}\text{Fe}_{20}$, and (c) Ni, respectively. The electrical current density was (i) 10×10^7 A/cm², (ii) 15×10^7 A/cm², and (iii) 20×10^7 A/cm² for $\text{Co}_{90}\text{Fe}_{10}$ in Fig. 3a, and (i) 1.5×10^7 A/cm², (ii) 3.5×10^7 A/cm², (iii) and 6.0×10^7 A/cm² for $\text{Ni}_{80}\text{Fe}_{20}$ and Ni in Fig. 3b,c. Furthermore, we tuned the current density to obtain the stable STO considering this depends on the top layer materials, as previously discussed. The calculated data under the wide current density, including Fig. 3, are also shown in Fig. S1, S2 and S3 in Supplementary material.

We now focus on the time domains when the current density is increased, as shown in Fig. 3b,c [(i)–(iii)]. For all top layers, an STO was observed with a B_{12} of either 0.0 or -0.6 at a relatively low current density, shown in (i). However, as shown in (ii) and (iii), as the current density increased, the stable STO with an almost immutable

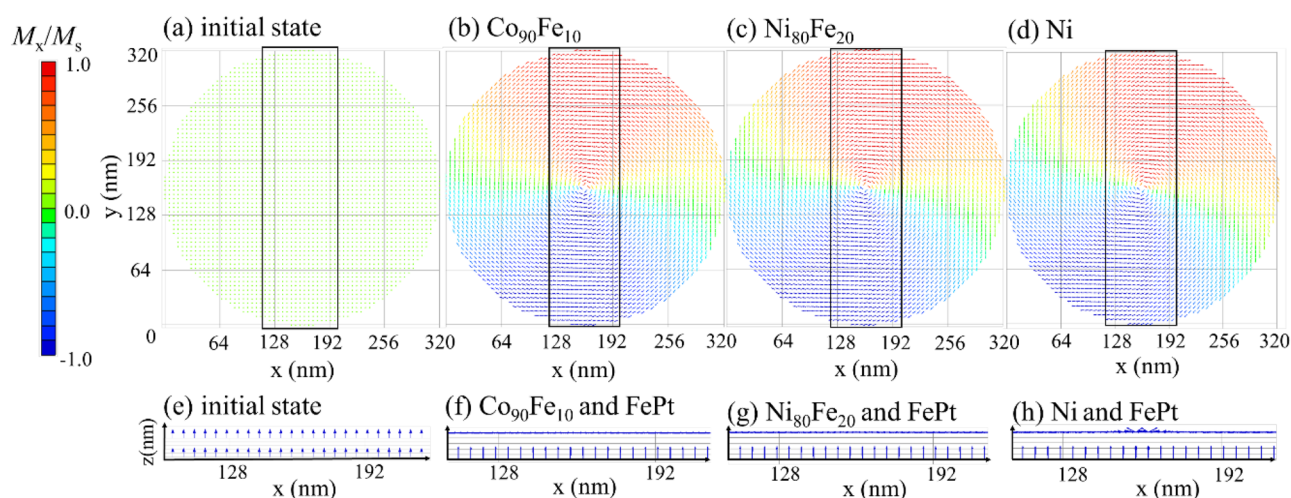


Figure 2. [Top] Top views of the magnetization configuration of the top layers for (a) the initial state of z -axis magnetization saturation for $\text{Co}_{90}\text{Fe}_{10}$ 2 nm, (b) the relaxed state of $\text{Co}_{90}\text{Fe}_{10}$ 2 nm, (c) the relaxed state of $\text{Ni}_{80}\text{Fe}_{20}$ 2 nm, and (d) the relaxed state of Ni 2 nm when $A_{12} = 0$ and $B_{12} = -0.6$. In the initial state, the configuration does not depend on the material of the top layer. [Bottom] Side views of the magnetization configuration in bottom FePt 2 nm/spacer 2 nm/top layer 2 nm when the top layer is (a) the $\text{Co}_{90}\text{Fe}_{10}$ 2 nm in the initial state, (b) the relaxed state of $\text{Co}_{90}\text{Fe}_{10}$ 2 nm, (c) the relaxed state of $\text{Ni}_{80}\text{Fe}_{20}$ 2 nm, and (d) the relaxed state of Ni 2 nm, corresponding to the enclosed area in (e–h). The top and bottom arrows show the magnetization of the top and bottom layers, respectively. Magnetic moments in the y -direction are superimposed on each x position.

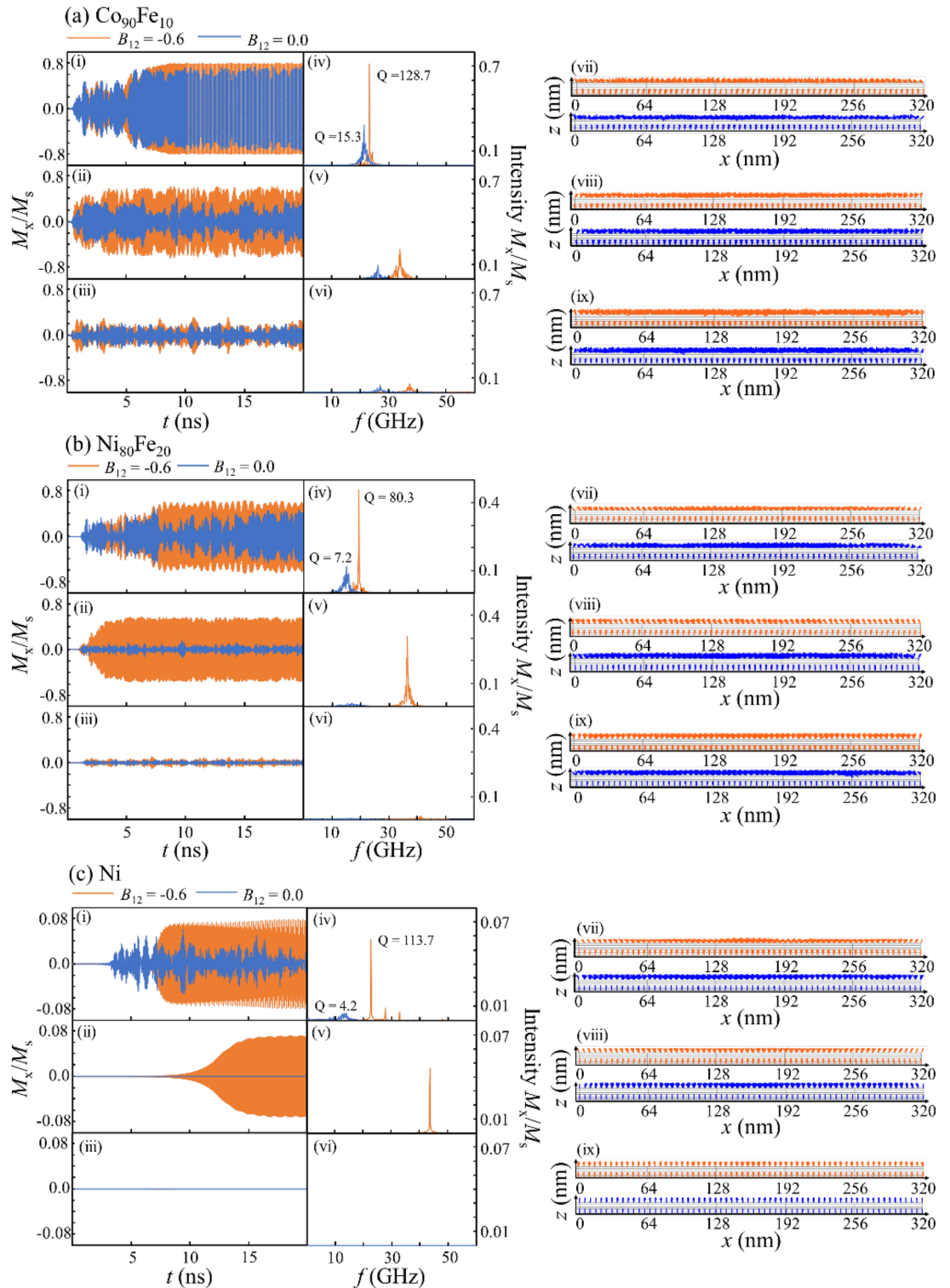


Figure 3. STO performances for the top layer of (a) Co₉₀Fe₁₀, (b) Ni₈₀Fe₂₀, and (c) Ni in the orthogonal configuration with an out-of-plane initial state, namely the z-axis. (i–iii) Time-domain magnetization precessions M_x/M_s , (iv–vi) Fast Fourier transform spectra, and (vii)–(ix) side views of magnetization configuration. The light blue and orange lines denote the results for $B_{12} = 0.0$ and $B_{12} = -0.6$, respectively. For the time-domain magnetization precessions M_x/M_s , the electrical current density was (i) 10×10^7 A/cm², (ii) 15×10^7 A/cm², and (iii) 20×10^7 A/cm² for Co₉₀Fe₁₀, and (i) 1.5×10^7 A/cm², (ii) 3.5×10^7 A/cm², and (iii) 6.0×10^7 A/cm² for Ni₈₀Fe₂₀ and Ni.

M_x/M_s is lost; in other words, the degradation of M_x/M_s when $B_{12}=0.0$ is larger compared to when $B_{12}=-0.6$. This means that by introducing biquadratic magnetic coupling, we can expand the electric current region where the stable STO is realized. Therefore, the current density can be increased, which results in a high frequency in the STO. Additionally, the FFT spectra in (iv)–(vi) show that the STO frequency is higher for $B_{12}=-0.6$ than $B_{12}=0.0$, even for the same current density. We also calculate the quality factor Q . The FFT curve was fitted with a Gaussian distribution while changing the standard deviation σ . The quality factor was derived from the FWHM of the fitting curve when the residual error between Gaussian distribution curve and FFT curve is minimum. Since the quality factor Q increased by introducing B_{12} , the extrinsic disturbance decreased and the ideal frequency became evident, resulting in a high STO frequency. This was supported by the side views of the magnetization in (vii)–(ix). The variation of magnetization precession angle of the top layer is larger when $B_{12}=0.0$ than $B_{12}=-0.6$ for the same current density in the same top layer materials. Moreover, the variation of the precession angle led to a poor Q factor. The detail comparison of angle variation is shown in Supplementary material.

Changing the top layer from $\text{Co}_{90}\text{Fe}_{10}$ and $\text{Ni}_{80}\text{Fe}_{20}$ to Ni, M_s becomes a small value and the current density required to realize the STO can be reduced. The combination of biquadratic coupling and M_s reduction is another possible approach for improving the frequency, as reported in Ref.⁶¹

In conclusion, we revealed the STO characteristics in an orthogonal magnetization sample with biquadratic coupling. We found that the transient time until the stable STO was approximately 5–15 ns, which is too long for oscillators to be ignored. Therefore, in the following, we find the optimal initial state for a short transient time.

Static and dynamic properties with y-axis magnetization saturation in initial state. Figure 4a shows the initial magnetization state before relaxation, where the magnetization of the top layer is saturated in-plane, *i. e.*, the y -axis, by a sufficient external field. The calculated magnetization maps after relaxation in the top layers, $\text{Co}_{90}\text{Fe}_{10}$, $\text{Ni}_{80}\text{Fe}_{20}$, and Ni, are shown in Fig. 4b–d, respectively, when neither external fields nor electrical currents were applied. All layers exhibited typical magnetic domains with in-plane magnetization, *i. e.*, a single domain or onion domain, with a domain wall where the magnetization gradually rotated. Technically, only the $\text{Co}_{90}\text{Fe}_{10}$ top layer had an onion domain; the $\text{Ni}_{80}\text{Fe}_{20}$ and Ni top layers exhibited a single domain with magnetization at an angle of 45° from the x -axis owing to the difference in the magnetostatic energy that varied with the saturation of the magnetization. On comparing Figs. 2 and 4, we see that the relaxed top layer magnetization structure depends on whether the magnetization was initially saturated on the z -axis or y -axis. The side views of the magnetization configuration of the top and bottom layers are shown in Fig. 4e–g. The magnetization of the bottom layers of the three materials were along the z -axis, and the magnetization of the top layers were oriented along the xy -plane, forming an orthogonal configuration. The orthogonal structure was regularly obtained regardless of the initial state prior to relaxation.

Next, we considered the dynamics when the current flows through the device from the top to the bottom layers, similar to the case of initial state with z -axis magnetization saturation in the previous section. Figure 5a–c show the [(i–iii)] time-domain magnetization precession, [(iv–vi)] Fast Fourier transform (FFT) spectra, and [(vii–ix)] side view snapshots of the magnetization configuration of the top and bottom layers at 10 ns after the current flow, with B_{12} is 0.0 or -0.6 , for (a) $\text{Co}_{90}\text{Fe}_{10}$, (b) $\text{Ni}_{80}\text{Fe}_{20}$, and (c) Ni. The electrical current densities were set as the same values as those for the z -axis saturation at the initial state in the previous section. The calculated data under the wide current density, including Fig. 5, are also shown in Fig. S4, S5 and S6 in Supplementary

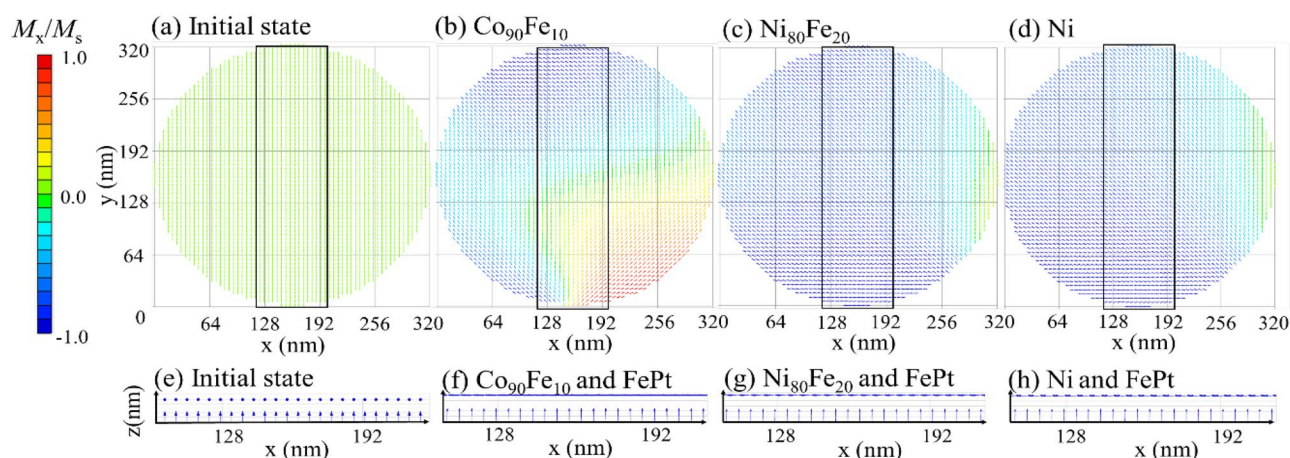


Figure 4. [Top] Top views of the magnetization configuration of the top layers for (a) the initial state of y -axis magnetization saturation for $\text{Co}_{90}\text{Fe}_{10}$ 2 nm, (b) the relaxed state of $\text{Co}_{90}\text{Fe}_{10}$ 2 nm, (c) the relaxed state of $\text{Ni}_{80}\text{Fe}_{20}$ 2 nm, and (d) the relaxed state of Ni 2 nm when $A_{12}=0$ and $B_{12}=-0.6$. In the initial state, the configuration does not depend on the material of the top layer. [Bottom] Side views of magnetization configuration in bottom FePt 2 nm/spacer 2 nm/top layer 2 nm when the top layer is (a) the $\text{Co}_{90}\text{Fe}_{10}$ 2 nm in the initial state, (b) the relaxed state of $\text{Co}_{90}\text{Fe}_{10}$ 2 nm, (c) the relaxed state of $\text{Ni}_{80}\text{Fe}_{20}$ 2 nm, and (d) the relaxed state of Ni 2 nm, corresponding to the enclosed area in (e–h). The top and bottom arrows show the magnetization of the top and bottom layers, respectively. Magnetic moments in the y -direction are superimposed on each x position.

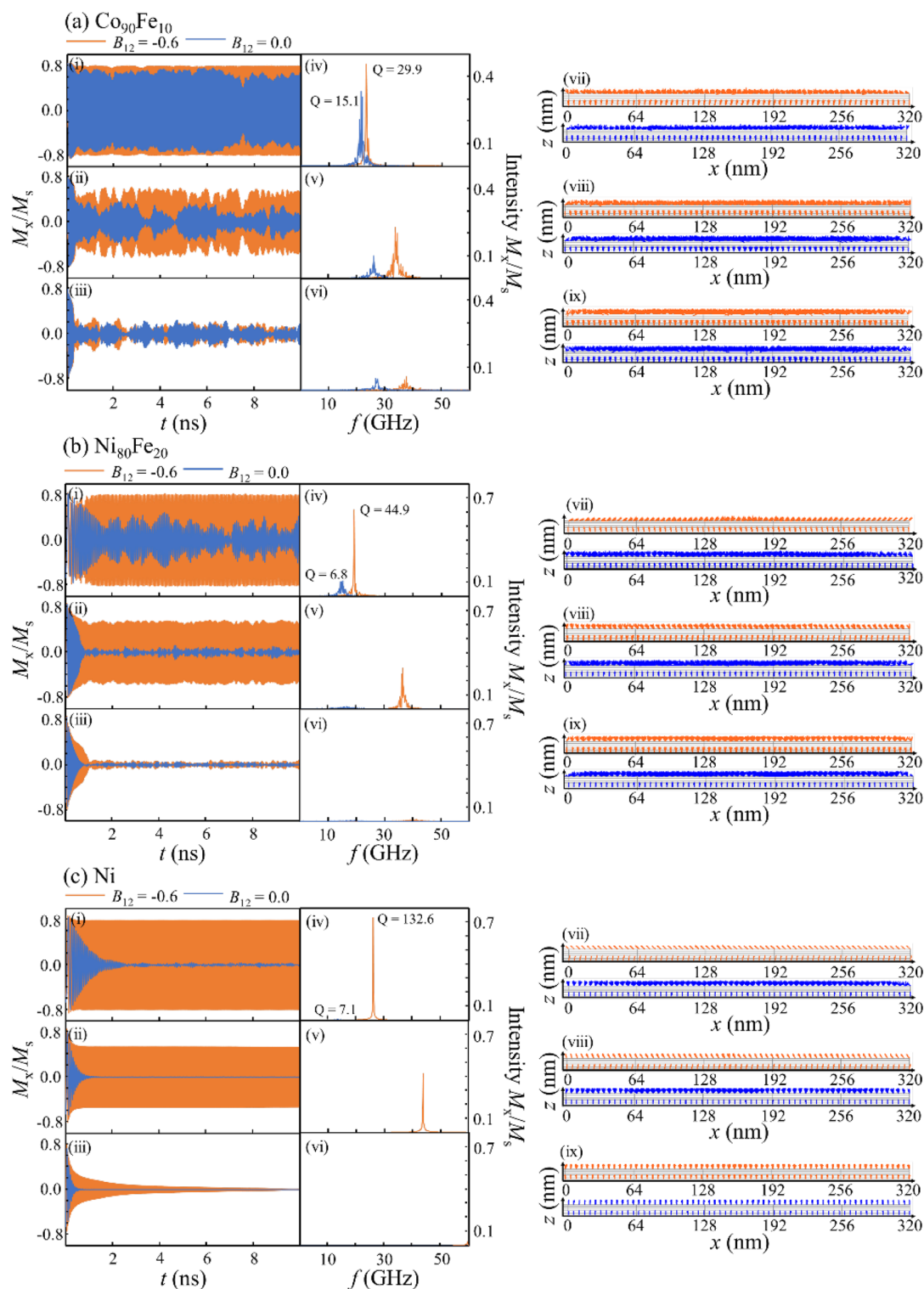


Figure 5. STO performances for the top layer of (a) $\text{Co}_{90}\text{Fe}_{10}$, (b) $\text{Ni}_{80}\text{Fe}_{20}$, and (c) Ni in the orthogonal configuration with an out-of-plane initial state, namely the y -axis. (i–ii) Time-domain magnetization precessions M_x/M_s , (iv–vi) the Fast Fourier transform spectra, and (vii–ix) side views of magnetization configuration. The light blue and orange lines denote the results for $B_{12} = 0.0$ and $B_{12} = -0.6$, respectively. For the time-domain magnetization precessions M_x/M_s , the electrical current density was (i) 10×10^7 A/cm², (ii) 15×10^7 A/cm², and (iii) 20×10^7 A/cm² for $\text{Co}_{90}\text{Fe}_{10}$, and (i) 1.5×10^7 A/cm², (ii) 3.5×10^7 A/cm², and (iii) 6.0×10^7 A/cm² for $\text{Ni}_{80}\text{Fe}_{20}$ and Ni.

material. The common tendencies were obtained in both initial states of y -axis and z -axis saturation; the sample with $B_{12} = -0.6$ exhibited a more stable STO with an almost immutable M_x/M_s , a higher quality factor Q , and higher frequency than that with $B_{12} = 0.0$. We found that the biquadratic coupling is effective for increasing the frequency, regardless of the initial state.

However, there is a clear difference in the transient time between the initial state with y -axis and z -axis magnetization saturation. For the initial state with z -axis saturation magnetization, the transient times were 5.5, 8.9, and 11.2 ns for $\text{Co}_{90}\text{Fe}_{10}$, $\text{Ni}_{80}\text{Fe}_{20}$, and Ni, respectively, as shown in Fig. 3. In contrast, for the initial state with y -axis saturation magnetization, the transient times were 0.7, 1.2, and 1.0 ns for $\text{Co}_{90}\text{Fe}_{10}$, $\text{Ni}_{80}\text{Fe}_{20}$, and Ni, respectively, as shown in Fig. 5. Therefore, the transient time was significantly reduced by changing the initial magnetization state. As an example, we have provided a video of the magnetic moment dynamics for the Ni layer under $3.0 \times 10^7 \text{ A/cm}^2$ for the initial states of z -axis and y -axis saturation (see the Supplementary material).

Notably, we can see a long period fluctuation in the time domain of the STO in Figs. 3a–c and 5a and b. This explains the overlapping of several STO modes, as shown in the [(iv–vi)] FFT spectra and [(vii–ix)] side views of the magnetization. For the Ni top layer only, there was one peak in the FFT and the magnetization amplitude was relatively uniform because of its small M_s .

Once the STO was obtained, the effect of the initial state on the STO frequency was found to be insignificant. However, for Ni only, the magnitude of M_x/M_s was increased from 0.084 to 0.800 by changing the initial state from z -axis saturation to y -axis saturation, as shown in Figs. 3c and 5c. This indicates that the initial magnetization state affects the transient time as well as the STO intensity when the top layer is Ni. To determine the reason for the large change in M_x/M_s only for Ni, we compared the side view snapshots of the magnetization between the two different the initial states in Figs. 3c and 5c. In Fig. 3c, the magnetization directions of the top Ni layer disperse in the xy -plane, which indicates that the trajectory of magnetization is not uniform in the film, which decreases the total intensity M_x/M_s . On the other hand, as shown in Fig. 5c, the magnetization directions of the top layer maintain the same direction, leading to a large total intensity M_x/M_s . We observed that the magnetization directions disperse in the xy -plane, but the z component of the total magnetization does not depend on the initial magnetization state, which will be explained in the followings.

Effect of initial state and biquadratic coupling on the STO. Figure 6 shows the STO frequency, intensity M_x/M_s , and transient time as a function of the current density for the initial states of z -axis and y -axis saturation. The M_x/M_s intensity over 0.1 is plotted. The solid circle and triangle denote the results for the initial states of y -axis saturation when B_{12} is -0.6 and 0.0 , respectively. The open square and diamond denote the calculated results for the initial states of z -axis saturation when B_{12} is -0.6 and 0.0 , respectively. In both cases, the critical current density for realizing the STO decreases and the frequency increases by changing the top layer from $\text{Co}_{90}\text{Fe}_{10}$ to $\text{Ni}_{80}\text{Fe}_{20}$ and Ni, depending on their M_s . Provided the saturation magnetization does not change, the intensity M_x/M_s decreases with an increase in current density. Whether the top layer is Ni, $\text{Ni}_{80}\text{Fe}_{20}$, or $\text{Co}_{90}\text{Fe}_{10}$, the current density region realizing the stable STO is widened by using $B_{12} = -0.6$ instead of $B_{12} = 0$. In particular, the biquadratic coupling effect is most obvious in the top layer of Ni, whose saturation magnetization is small when the initial state is y -axis saturation. There appears to be no significant difference in the frequencies and intensity of M_x/M_s dependencies on the current density between the two initial states, except for Ni, which is consistent with the comparison results between Figs. 3c and 5c. In contrast to the frequency and intensity, a large discrepancy is observed in the transient times between the two initial states, as shown in Fig. 6c. Regardless of the current flow in any of the top layers, the initial state with y -axis saturation demonstrated a much smaller transient time than in the initial state with z -axis saturation. This tendency is particularly pronounced in the $\text{Ni}_{80}\text{Fe}_{20}$ and Ni top layers with an M_s smaller than that of $\text{Co}_{90}\text{Fe}_{10}$. We noted that the transient time did not change as the current density changed for an initial state of y -axis saturation; however, it varied widely for an initial state of z -axis saturation. This large variation in the transient time can be attributed to the dispersion of the magnetization directions in the xy -plane, as shown in the side views.

Finally, to confirm the effect of biquadratic coupling on STO performance, we compare the frequency, intensity, and transient time between the system with and without biquadratic coupling, namely between $B_{12} = -0.6$ and $B_{12} = 0$, highlighted by solid triangles and open diamonds in Fig. 6, respectively. The biquadratic coupling clearly increases the STO frequency for the same current density. However, more importantly, the current density region for which the STO was realized was expanded by the biquadratic coupling, resulting in the possibility that the maximum value of the frequency could be increased.

Conclusion

In summary, we carried out a numerical investigation on spin torque oscillation in the magnetic multilayer FePt/spacer/ $\text{Co}_{90}\text{Fe}_{10}$, $\text{Ni}_{80}\text{Fe}_{20}$, or Ni with an orthogonal magnetization configuration by introducing biquadratic magnetic coupling. The frequency and current density region were increased by introducing the biquadratic coupling, leading to 37 GHz, 40 GHz, and 58 GHz in the $\text{Co}_{90}\text{Fe}_{10}$, $\text{Ni}_{80}\text{Fe}_{20}$ and Ni layer at a current density of $18 \times 10^7 \text{ A/cm}^2$, $4 \times 10^7 \text{ A/cm}^2$, and $5.5 \times 10^7 \text{ A/cm}^2$, respectively. In addition, we determined that two types of initial magnetic state, z -axis saturation and y -axis saturation, result in a vortex structure and in-plane onion magnetic structure after relaxation, respectively. The transient time before the stable STO was reduced from 0.5 to 1.8 ns by changing the initial state from z -axis saturation to y -axis saturation. The vortex structure is more stable than the onion structure, which is considered to be the reason for the difference in the transient time. By combining the orthogonal configuration, the biquadratic magnetic coupling, and the initial state with in-plane magnetic saturation, a stable STO with several tens of GHz frequency was obtained, which is advantageous for STO applications.

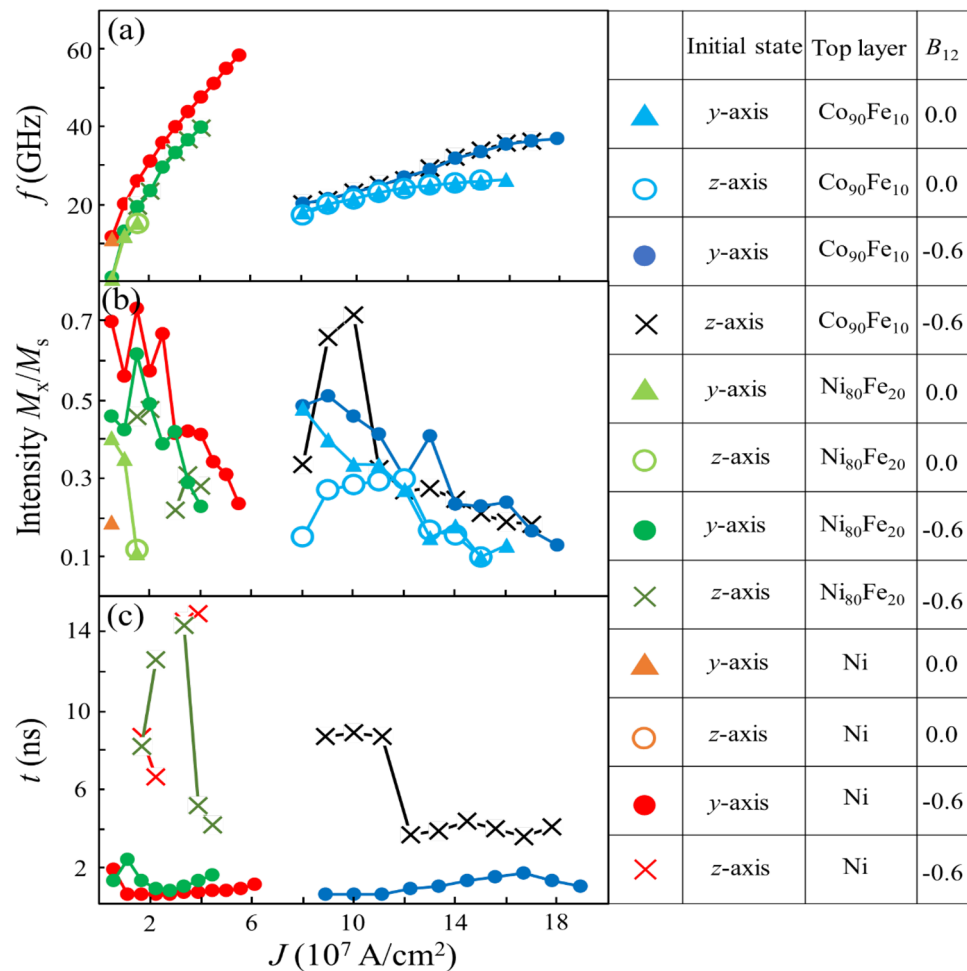


Figure 6. Current density dependences of (a) frequency, (b) intensity M_x/M_s , and (c) transient time in an orthogonal configuration. The solid circles and triangles denote the calculated results for the initial states of y-axis saturation when B_{12} is -0.6 or 0.0 , respectively. The open squares and diamonds denote the calculated results for the initial states of z-axis saturation when B_{12} is -0.6 or 0.0 , respectively.

Data availability

All data generated or analyzed during this study are included in this published article and its Supplementary Information files. The datasets used and/or analyzed during the current study available from the corresponding author on reasonable request.

Received: 20 October 2022; Accepted: 2 March 2023

Published online: 03 March 2023

References

- Slonczewski, J. C. Current-driven excitation of magnetic multilayers. *J. Magn. Magn. Mater.* **159**, L1 (1996).
- Berger, L. Emission of spin waves by a magnetic multilayer traversed by a current. *Phys. Rev. B* **54**, 9353 (1996).
- Zhu, J., Zhu, X. & Tang, Y. Microwave assisted magnetic recording. *IEEE Trans. Magn.* **44**, 125 (2008).
- Zhu, J. & Wang, Y. Microwave assisted magnetic recording utilizing perpendicular spin torque oscillator with switchable perpendicular electrodes. *IEEE Trans. Magn.* **46**, 751 (2010).
- Igarashi, S. M., Suzuki, Y., Miyamoto, H. & Shiro, Y. Effective write field for microwave assisted magnetic recording. *IEEE Trans. Magn.* **46**, 2507 (2010).
- Narita, N. *et al.* Analysis of effective field gradient in microwave-assisted magnetic recording. *IEEE Trans. Magn.* **50**, 3203004 (2014).
- Hosomi, M. *et al.* A novel nonvolatile memory with spin torque transfer magnetization switching: Spin-RAM, IEEE Int. Electron Devices Meeting (IEDM) Tech. Dig. 459 (2005).
- Apalkov, S. *et al.* Spin-transfer torque magnetic random access memory (STT-MRAM). *ACM J. Emerg. Technol. Comput. Syst.* **9**, 1 (2013).
- Romera, M. *et al.* Vowel recognition with four coupled spin-torque nano-oscillators. *Nature* **563**, 230 (2018).
- Arai, H. & Imamura, H. Neural-network computation using spin-wave-coupled spin-torque oscillators. *Phys. Rev. Appl.* **10**, 024040 (2018).
- Tsunegi, S. *et al.* Evaluation of memory capacity of spin torque oscillator for recurrent neural networks. *Jpn. J. Appl. Phys.* **57**, 120307 (2018).

12. Kiselev, S. I. *et al.* Microwave oscillations of a nanomagnet driven by a spin-polarized current. *Nature* **425**, 380 (2003).
13. Rippard, W. H., Pufall, M. R., Kaka, S., Russek, S. E. & Silva, T. J. Time-resolved reversal of spin-transfer switching in a nanomagnet. *Phys. Rev. Lett.* **92**, 088302 (2004).
14. Okura, R. *et al.* High-power rf oscillation induced in halfmetallic Co₂MnSi layer by spin-transfer torque. *Appl. Phys. Lett.* **99**, 052510 (2011).
15. Stiles, M. D. & Zangwill, A. Anatomy of spin-transfer torque. *Phys. Rev. B* **66**, 014407 (2002).
16. Núñez, A. S., Duine, R. A., Haney, P. & MacDonald, A. H. Theory of spin torques and giant magnetoresistance in antiferromagnetic metals. *Phys. Rev. B* **73**, 214426 (2006).
17. Wei, Z. *et al.* Changing exchange bias in spin valves with an electric current. *Phys. Rev. Lett.* **98**, 116603 (2007).
18. Urazhdin, S. & Anthony, N. Effect of polarized current on the magnetic state of an antiferromagnet. *Phys. Rev. Lett.* **99**, 046602 (2007).
19. Haney, P. M. & MacDonald, A. H. Current-induced torques due to compensated antiferromagnets. *Phys. Rev. Lett.* **100**, 196801 (2008).
20. Wei, Z., Basset, J., Sharma, A., Bass, J. & Tsoi, M. Spin-transfer interactions in exchange biased spin valves. *J. Appl. Phys.* **105**, 07D108 (2009).
21. Moriyama, T. *et al.* Anti-damping spin transfer torque through epitaxial nickel oxide. *Appl. Phys. Lett.* **106**, 162406 (2015).
22. Yamane, Y., Ieda, J. & Sinova, J. Spin-transfer torques in antiferromagnetic textures: Efficiency and quantification method. *Phys. Rev. B* **94**, 054409 (2016).
23. Jungwirth, T. *et al.* The multiple direction of antiferromagnetic spintronics. *Nat. Phys.* **14**, 200 (2018).
24. Chen, X. Z. *et al.* Antidamping-torque-induced switching in biaxial antiferromagnetic insulators. *Phys. Rev. Lett.* **120**, 207204 (2018).
25. Roschewsky, N. *et al.* Spin-orbit torques in ferrimagnetic GdFeCo alloys. *Appl. Phys. Lett.* **109**, 112403 (2016).
26. Lisenkov, I., Khymyn, R., Åkerman, J., Sun, N. X. & Ivanov, B. A. Subterahertz ferrimagnetic spin-transfer torque oscillator. *Phys. Rev. B* **100**, 100409(R) (2019).
27. Okuno, T. *et al.* Spin-transfer torques for domain wall motion in antiferromagnetically coupled ferrimagnets. *Nat. Electron.* **2**, 389 (2019).
28. Khymyn, R., Lisenkov, I., Tiberkevich, V., Ivanov, B. & Slavin, A. Antiferromagnetic THz-frequency Josephson-like oscillator driven by spin current. *Sci. Rep.* **7**, 43705 (2017).
29. Puliafito, V. *et al.* Micromagnetic modeling of terahertz oscillations in an antiferromagnetic material driven by the spin Hall effect. *Phys. Rev. B* **99**, 024405 (2019).
30. Seki, T., Tomita, H., Shiraishi, M., Shinjo, T. & Suzuki, Y. Coupled-mode excitations induced in an antiferromagnetically coupled multilayer by spin-transfer torque. *Appl. Phys. Express* **3**, 033001 (2010).
31. Zhong, H. *et al.* Terahertz spin-transfer torque oscillator based on a synthetic antiferromagnet. *J. Magn. Magn. Mater.* **497**, 166070 (2020).
32. Volvach, I., Kent, A. D., Fullerton, E. E. & Lomakin, V. Spin-transfer-torque oscillator with an antiferromagnetic exchange-coupled composite free layer. *Phys. Rev. Appl.* **18**, 024071 (2022).
33. Nagashima, G. *et al.* Quasi-antiferromagnetic multilayer stacks with 90° coupling mediated by thin Fe oxide spacers. *J. Appl. Phys.* **126**, 093901 (2019).
34. Horiike, S., Nagashima, G., Kurokawa, Y., Zhong, Y., Yamanoi, K., Tanaka, T., Matsuyama, K., and Yuasa, H., Magnetic dynamics of quasi-antiferromagnetic layer fabricated by 90° magnetic coupling. *Jpn. J. Appl. Phys.* **59**, SGGI02 (2020).
35. Seki, T., Mitani, S., Yakushiji, K. & Takanashi, K. Magnetization reversal by spin-transfer torque in 90° configuration with a perpendicular spin polarizer. *Appl. Phys. Lett.* **89**, 172504 (2006).
36. Houssameddine, D. *et al.* Spin-torque oscillator using a perpendicular polarizer and a planar free layer. *Nat. Mater.* **6**, 447 (2007).
37. Liu, H., Bedau, D., Backes, D., Katine, J. A. & Kent, A. D. Ultrafast switching in magnetic tunnel junction based orthogonal spin transfer devices. *Appl. Phys. Lett.* **97**, 242510 (2010).
38. Liu, H., Bedau, D., Backes, D., Katine, J. A. & Kent, A. D. Precessional reversal in orthogonal spin transfer magnetic random access memory devices. *Appl. Phys. Lett.* **101**, 032403 (2012).
39. Suto, H. *et al.* Magnetization dynamics of a MgO-based spin-torque oscillator with a perpendicular polarizer layer and a planar free layer. *J. Appl. Phys.* **112**, 083907 (2012).
40. Kubota, H. *et al.* Spin-torque oscillator based on magnetic tunnel junction with a perpendicularly magnetized free layer and in-plane magnetized polarizer. *Appl. Phys. Express* **6**, 103003 (2013).
41. Rahman, N. & Sbiaa, R. Thickness dependence of magnetization dynamics of an in-plane anisotropy ferromagnet under a crossed spin torque polarizer. *J. Magn. Magn. Mater.* **439**, 95 (2017).
42. Liu, C. *et al.* Spin transfer torque oscillation in orthogonal magnetization disks. *IEEE Trans. Magn.* **58**, 4100305 (2021).
43. Slonczewski, J. C. Fluctuation mechanism for biquadratic exchange coupling in magnetic multilayers. *Phys. Rev. Lett.* **67**, 3172 (1991).
44. Fuss, A., Demokritov, S., Grünberg, P. & Zinn, W. Short and long period oscillations in the exchange coupling of Fe across epitaxially grown Al and Au interlayers. *J. Magn. Magn. Mater.* **103**, L221 (1992).
45. Gutierrez, C. J., Krebs, J. J., Flipkowski, M. E. & Prinz, G. A. Strong temperature dependence of the 90° coupling in Fe/Al/Fe (001) magnetic trilayers. *J. Magn. Magn. Mater.* **116**, L305 (1992).
46. Heinrich, B. *et al.* Bilinear and biquadratic exchange coupling in bcc Fe/Cu/Fe trilayers: Ferromagnetic-resonance and surface magneto-optical Kerr-effect studies. *Phys. Rev. B* **47**, 5077 (1993).
47. Slonczewski, J. C. Overview of interlayer exchange theory. *J. Magn. Magn. Mater.* **150**, 13 (1995).
48. Filipkowski, M. E., Krebs, J. J., Prinz, G. A. & Gutierrez, C. J. Giant bear-90° coupling in epitaxial CoFe/Mn/CoFe sandwich structures. *Phys. Rev. Lett.* **75**, 1847 (1995).
49. Demokritov, S. O. Biquadratic interlayer coupling in layered magnetic systems. *J. Phys. D: Appl. Phys.* **31**, 925 (1998).
50. Heijden, P. A. A. *et al.* Evidence for roughness driven 90± coupling in Fe₃O₄/NiO/Fe₃O₄ trilayers. *Phys. Rev. Lett.* **82**, 1020 (1999).
51. Yana, S.-S., Grünberg, P. & Mei, L.-M. Magnetic phase diagrams of the trilayers with the noncollinear coupling in the form of the proximity magnetism model. *J. Appl. Phys.* **88**, 983 (2000).
52. Wang, H. *et al.* Oscillatory interlayer exchange coupling in epitaxial Co₂MnSi/Cr/Co₂MnSi trilayers. *Appl. Phys. Lett.* **90**, 142510 (2007).
53. Fukuzawa, H. *et al.* Specular spin-valve films with an FeCo nano oxide layer by ion-assisted oxidation. *J. Appl. Phys.* **91**, 6684 (2002).
54. Lai, C. H. & Lu, K. H. Biquadratic coupling through nano-oxide layers in pinned layers of IrMn-based spin valves. *J. Appl. Phys.* **93**, 8412 (2003).
55. Zhong, Y. *et al.* Determination of fine magnetic structure of magnetic multilayer with quasi antiferromagnetic layer by using polarized neutron reflectivity analysis. *AIP Adv.* **10**, 015323 (2020).
56. Belmuguenai, M., Martin, T., Woltersdorf, G., Maier, M. & Bayreuther, G. Frequency- and time-domain investigation of the dynamic properties of interlayer-exchange coupled Ni₈₁Fe₁₉/Ru/Ni₈₁Fe₁₉ thin films. *Phys. Rev. B* **76**, 104414 (2007).
57. Tanaka, Y., Saita, S. & Maenosono, S. Influence of surface ligands on saturation magnetization of FePt nanoparticles. *Appl. Phys. Lett.* **92**, 093117 (2008).

58. Shima, T., Takanashi, K., Takahashi, Y. K. & Hono, K. Preparation and magnetic properties of highly coercive FePt films. *Appl. Phys. Lett.* **81**, 1050 (2002).
59. Bonin, R., Schneider, M. L., Silva, T. J. & Nibarger, J. P. Dependence of magnetization dynamics on magnetostriction in NiFe alloys. *J. Appl. Phys.* **98**, 123904 (2005).
60. Venkatesh, M., Ramakanth, S., Chaudhary, A. K. & James Raju, K. C. Study of terahertz emission from Ni films of different thicknesses using ultrafast laser pulses. *Opt. Mater. Express* **6**, 2342 (2016).
61. Kurokawa, Y. *et al.* Ultra-wide-band millimeter-wave generator using spin torque oscillator with strong interlayer exchange couplings. *Sci. Rep.* **12**, 10849 (2022).

Acknowledgements

This study was supported by the Japan Society for the Promotion of Science KAKENHI (Grant No. JP19K04471, JP22H01557), Micron Foundation, the Mitsubishi Foundation, the Center for Spintronics Research Network (Osaka), and JST, the establishment of university fellowships towards the creation of science technology innovation, Grant Number JPMJFS2132.

Author contributions

C.L., Y.K. and H.Y. planned the project. C.L., K.Y., N.H. and T.T. established micromagnetic simulator. C.L. carried out micromagnetic simulations. H.Y. supervised the project.

Competing interests

The authors declare no competing interests.

Additional information

Supplementary Information The online version contains supplementary material available at <https://doi.org/10.1038/s41598-023-30838-y>.

Correspondence and requests for materials should be addressed to C.L.

Reprints and permissions information is available at www.nature.com/reprints.

Publisher's note Springer Nature remains neutral with regard to jurisdictional claims in published maps and institutional affiliations.



Open Access This article is licensed under a Creative Commons Attribution 4.0 International License, which permits use, sharing, adaptation, distribution and reproduction in any medium or format, as long as you give appropriate credit to the original author(s) and the source, provide a link to the Creative Commons licence, and indicate if changes were made. The images or other third party material in this article are included in the article's Creative Commons licence, unless indicated otherwise in a credit line to the material. If material is not included in the article's Creative Commons licence and your intended use is not permitted by statutory regulation or exceeds the permitted use, you will need to obtain permission directly from the copyright holder. To view a copy of this licence, visit <http://creativecommons.org/licenses/by/4.0/>.

© The Author(s) 2023